

Intrinsic carrier concentration and minority-carrier mobility of silicon from 77 to 300 K

A. B. Sproul and M. A. Green

*Centre for Photovoltaic Devices and Systems, University of New South Wales, Kensington,
New South Wales 2033, Australia*

(Received 13 July 1992; accepted for publication 28 September 1992)

A considerable improvement in the accuracy of the measurement of the intrinsic carrier concentration in silicon near room temperature has recently been reported. This was achieved by the accurate analysis of minority-carrier current flow in specially fabricated p - n junction devices. In this paper this technique has been extended to measurements down to 77 K. A further improvement of the technique has been the simultaneous measurement of the minority-carrier electron mobility utilizing open-circuit voltage decay measurements.

I. INTRODUCTION

There is increasing interest in the operation and modeling of silicon metal-oxide-semiconductor and bipolar transistors at low temperatures.^{1,2} Low-temperature operation has the potential to improve the performance of devices without decreasing the feature size. The intrinsic carrier concentration n_i and the minority-carrier mobility μ are important parameters needed for the modeling of semiconductor properties and devices. Past measurements of n_i have been most accurately made at temperatures above 300 K. For example, the main technique used in the past to measure this parameter is based on intrinsic conductivity and mobility measurements.³ This technique has the greatest accuracy above 350 K where the purest of silicon samples available have intrinsic properties.³ This has meant that, in the range of 77–300 K, values of the intrinsic carrier concentration have relied upon calculations based on the band-gap energy and extrapolation of effective-mass measurements made at 4 K. The only other direct measurements reported in this temperature range are those by Herlet,⁴ from modeling of p - i - n diodes. However the results extend only as low as 250 K and recent measurements cast doubt on their accuracy.³ Therefore, the results presented here are the first direct measurement of the intrinsic carrier concentration in the temperature range below 250 K.

Most authors^{1,2} who calculate n_i in the low-temperature regime have relied on the effective-mass values reported by Barber.⁵ However, Barber's approach has been questioned by Madarasz, Lang, and Hemeger⁶ because Barber neglects the nonparabolicity of the heavy-hole band and treats the nonparabolicity of the light-hole band in an approximate fashion. This approach significantly underestimates the valence-band density-of-states effective mass m_{dv}^* at temperatures above 4 K.⁶ The more accurate values, as reported in a recent review by Green,³ are to be preferred; however, there is still some uncertainty with this approach due to the interpretation of the cyclotron resonance data at low temperatures and differences in methods of calculating the m_{dv}^* at higher temperatures. Therefore, to provide direct experimental data, we report in this article values of n_i determined from the analysis of minority-carrier current in narrow-base p - n junction diodes as a

function of temperature in the range 77–300 K. This method has already been successfully used to determine a value of $n_i = 1.00 \times 10^{10} \text{ cm}^{-3}$ at 300 K with an estimated one-standard-deviation uncertainty of only 3%.⁷ As an improvement over our previous study⁷ we also report minority-carrier electron mobility measurements made using the same device structure. This reduces a major source of uncertainty in the analysis. The mobility measurements were made using open-circuit voltage decay on these narrow-base devices.

The devices used in this study were based on the passivated emitter and rear solar cell (PERC). The PERC structure enabled the first silicon solar cells to be produced which surpassed 23% energy conversion efficiency.⁸ This high efficiency is possible due to the devices having near-ideal junction characteristics, low junction leakage, high postprocessing carrier lifetimes, and low recombination rates at surfaces and in diffused regions. These properties, as well as the large area of the devices (4 cm^2), makes them ideal for the measurements described here.

Modifications were made to the PERC design in order to simplify the modeling of the device characteristics. These have been described more fully in a paper describing measurements near room temperature.⁷ A schematic of the modified structure used in this study is shown in Fig. 1. The most important change to the design was to the rear metalization. In the PERC cells the rear surface is almost totally covered with a high-quality oxide which minimizes minority-carrier recombination. The rear electrical contact is made by small-area Al contacts to the p substrate through openings in the oxide. In the modified structure the passivating oxide is not included and the small-area Al contacts are replaced by an evaporated Al layer completely covering the wafer rear. This rear Al layer greatly simplifies the analysis of the devices characteristics as will be discussed in Sec. II. Subsequent processing of the device ensures that the only high-temperature treatment this Al layer receives is a standard subeutectic treatment at 400 °C for 5 min in a 5% H_2/N_2 atmosphere.⁸ All other aspects of the high-efficiency PERC structure were retained.

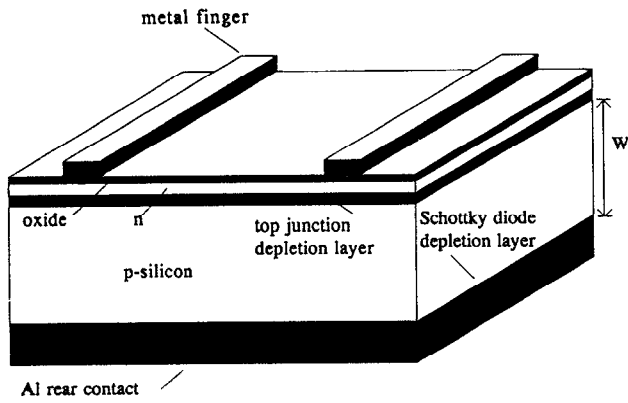


FIG. 1. The modified PERC silicon solar-cell structure. W is the width of the quasineutral p region.

II. THEORY

A. I - V characteristics

The PERC and the modified device structure used here have been modeled using standard semiconductor device theory.^{7,8} The illuminated I - V characteristics of the modified devices have been analyzed previously.⁷ The dark I - V characteristics were investigated in this study, and are derived in Appendix A. The devices can be described using a modified Ebers-Moll equivalent circuit for a bipolar transistor, shown in Fig. 2. The resulting expression that describes the forward-biased dark I - V characteristics is Eq. (A3) in Appendix A:

$$I = I_{01}(e^{q(V-IR')/kT} - 1) + I_{0n}(e^{q(V-IR')/nkT} - 1). \quad (1)$$

This expression is essentially the standard exponential relationship between current and voltage of a conventional

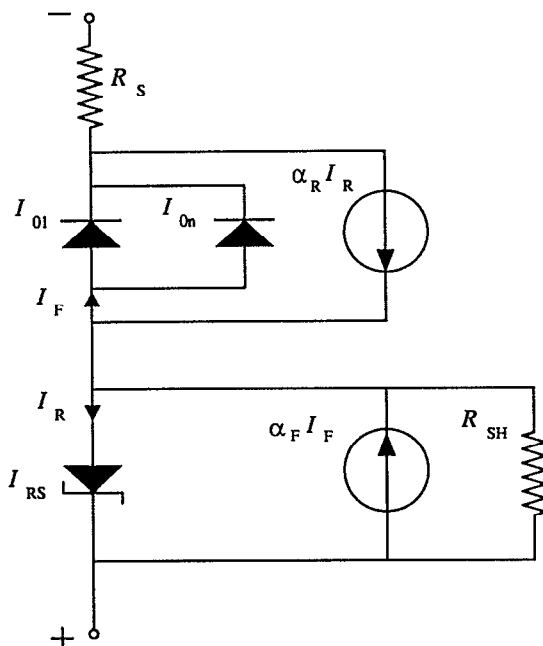


FIG. 2. Modified Ebers-Moll circuit which describes the PERC cell.

p - n diode. As discussed in Appendix A, the rear Al layer acts as a Schottky diode. This means that the device characteristics are more easily modeled than if the conventional passivated rear contact of the PERC structure were used. The basis of the method for determining the intrinsic carrier concentration is the following. Equation (1) was fitted to the experimental I - V characteristics and a value for the saturation current I_{01} was extracted. This quantity is strongly dependent on n_i .⁹ The intrinsic carrier concentration is then given by Eq. (A6) in Appendix A:

$$n_i = \left(\frac{WN_A^-(I_{01} - I_{0e})/1.025}{AqD_n(\omega \coth \omega)} \right)^{1/2}. \quad (2)$$

Hence, by measuring the saturation current I_{01} and the other parameters in Eq. (2), a value of n_i can be determined. The methods used to measure all parameters and the associated uncertainties are discussed in Sec. IV.

B. Open-circuit voltage decay (OCVD)

Open-circuit voltage decay was used to determine the minority-carrier electron diffusion constant in the base region of the devices. It is a technique that has been widely used in the study of lifetimes of minority carriers in p - n junction devices such as bipolar transistors and diodes. The basis of the method is to inject minority carriers into the device by forward biasing the diode. The current flow is then suddenly stopped and the device is open circuited. The injected minority carriers then recombine with a characteristic lifetime which causes the open-circuit voltage across the p - n junction to decay. In the simplest analysis, this decay is linear with a slope equal to $kT/q\tau_e$, where τ_e is the effective minority-carrier lifetime in the base region of the device.¹⁰

A more comprehensive treatment requires the solution of the time-dependent continuity equation. The relevant theory is outlined in Appendix B, which takes into account the effects of junction capacitance and emitter recombination on the open-circuit voltage decay (OCVD) signal. The important result for our purposes is that the decay can be characterized by a single decay time τ_0 given by

$$\frac{1}{\tau_0} = \frac{1}{\tau_b} + \left(\frac{\pi}{2W'} \right)^2 D_n, \quad (3)$$

where τ_b is the minority-carrier electron lifetime (or bulk lifetime) in the p region and W' is the effective width of the quasi-neutral p region. The effective width W' becomes less than the actual width W when recombination in the emitter region becomes significant. This can be calculated if the emitter saturation current I_{0e} is known, as outlined in Appendix B. Therefore, in conjunction with an estimate of the bulk lifetime τ_b , the minority-carrier electron diffusion constant D_n can be determined using Eq. (3). As will be shown below the bulk lifetimes of the devices investigated here are generally significantly larger than τ_0 introducing little uncertainty in the determination of D_n . All measurements were made with the devices in low injection. Hence, the minority carriers can be described by Boltzmann sta-

tistics and the diffusion constant can be related to the minority-carrier electron mobility by the Einstein relation ($D = \mu kT/q$).

III. EXPERIMENT

The substrates used were high-lifetime, float-zone, Wacker Chemitronic, (100) *p*-type, boron-doped silicon wafers with nominal resistivities of 10 and 2 Ω cm. The current-voltage (I - V) and the OCVD characteristics of the devices were investigated over the temperature range 77–300 K. The devices were mounted in a cryogenic system (Research and Manufacturing Company, model LTS-22-IR) which allows the temperature to be varied continuously over this range and held constant within less than 0.1 K. A silicon diode temperature sensor (Lake Shore) was mounted on the surface of the wafer to measure the temperature of the device. The diode was calibrated across the range of temperatures investigated against a calibrated Pt resistor (Lake Shore, model Pt-103). Resistance measurements were made using a Keithley 197 digital multimeter which was found to have an accuracy of 0.01% when calibrated against standards. This allowed the temperature measurements to be made with an accuracy of within 0.1 K. The wafers were clamped onto an Al block with a diameter of 70 mm, and thickness of 10 mm. This was then bolted directly onto the cold head of the cryogenic system. All wires internal to the cryogenic system were varnished copper with a diameter of 150 μ m, and were thermally anchored to minimize heat leakage from the ambient. A check on the results at temperatures near 77 K was made by submersing the devices in liquid nitrogen, and measuring the temperature with a calibrated Pt resistance sensor. The results of the device measurements, determined in this way, were in good agreement with the measurements made using the Cryogenic system.

A four-point probe arrangement was used for all I - V measurements. The meters used were Fluke 8842A digital multimeters, which were found to have an accuracy of 0.2% and 0.02% for the current and voltage measurements, respectively, when calibrated against standards. The OCVD measurements were made using a Hewlett Packard 54503A, 500 MHz digitizing oscilloscope. The devices were switched from forward bias to open circuit using a square-wave pulse generated by signal generator in series with a fast recovery blocking diode. When the input signal was positive the blocking diode was forward biased. When the input signal went negative the blocking diode ensured no current flowed and the device under test was at open circuit.

IV. RESULTS

A. I - V characteristics

The dark I - V characteristics of the devices were measured at temperatures between 77 and 300 K and are shown in Figs. 3 and 4. Equation (1) was fitted to the data with I_{01} , I_{0m} , n , and R' being the variable parameters. The analysis was confined to the data where the devices remained in low injection. Across the whole temperature

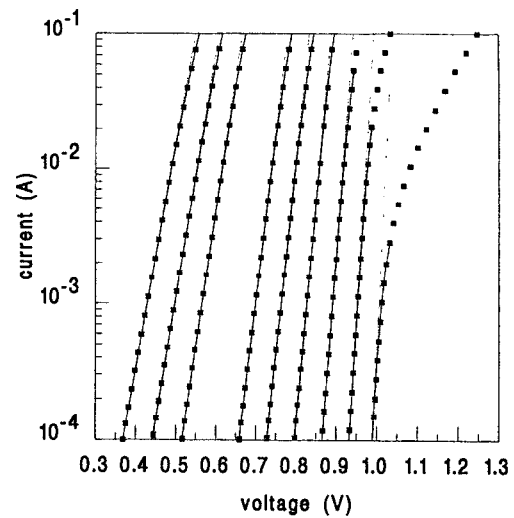


FIG. 3. Current-voltage characteristics of the 10 Ω cm device as a function of temperature (\blacksquare). The curves from left- to right-hand side are at the nominal temperatures of 300, 275, 250, 200, 175, 150, 125, 100, and 77 K. The exact temperatures are given in Table I. The solid line is a fitted curve while the dashed line is the ideal component of this fitted curve (ideality factor $n=1$).

range the data could be described to within $\sim 1\%$ by the fitted curve. Therefore, from these results the ideal component of the saturation current I_{01} could be extracted from the I - V characteristics of the devices with a high degree of certainty. The influence of the current component with an ideality factor $n > 1$ was negligible. This can be seen by the dominance of the ideal component of the current (ideality factor $n=1$) which is shown in Figs. 3 and 4 as the dashed line. The deviation of the experimental data, at higher cur-

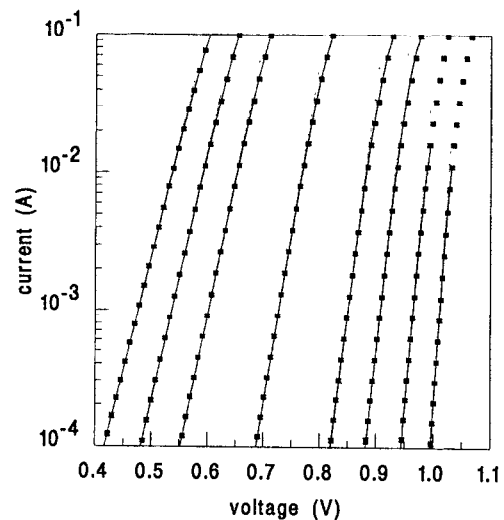


FIG. 4. Current-voltage characteristics of the 2 Ω cm device as a function of temperature (\blacksquare). The curves from left- to right-hand side are at the nominal temperatures of 300, 275, 250, 200, 150, 125, 100, and 77 K. The exact temperatures are given in Table II. The solid line is a fitted curve while the dashed line is the ideal component of this fitted curve (ideality factor $n=1$).

TABLE I. Saturation current I_{01} , ionized dopant density N_A^- , minority-carrier electron diffusion constant D_n , and diffusion length correction factor $\omega \coth \omega$, for the 10 Ω cm device, as a function of temperature from 77 to 300 K.

T (K)	I_{01} (A)	N_A^- (10^{15} cm^{-3})	D_n (cm^2/s)	$\omega \coth \omega$
77.4	$3.38(57) \times 10^{-69}$	0.81(16)	88.1(131)	1.018(18)
100.6	$2.11(31) \times 10^{-51}$	1.16(10)	84.0(118)	1.011(11)
125.9	$2.30(29) \times 10^{-39}$	1.27(8)	79.4(104)	1.007(7)
151.2	$2.84(31) \times 10^{-31}$	1.30(8)	71.7(88)	1.006(6)
200.3	$2.65(20) \times 10^{-21}$	1.31(8)	56.0(59)	1.004(4)
250.3	$4.17(20) \times 10^{-15}$	1.32(8)	43.0(38)	1.003(3)
275.3	$7.92(30) \times 10^{-13}$	1.32(8)	38.5(30)	1.003(3)
300.0	$5.94(17) \times 10^{-11}$	1.32(8)	34.7(24)	1.003(3)

rents and lower temperatures, away from the ideal curve, is predominantly due to the combined resistance of the series and rear shunt resistance as modeled by the effective resistance R' in Eq. (1). At lower temperatures this resistance increases as de-ionization of the acceptors in the base region increases. De-ionization also means that, as the temperature decreases, high injection occurs at currents that are lower than at higher temperatures. For some temperatures investigated, this introduces a current component with ideality factor $n > 1$ as the current increases. These departures away from the ideal are most noticeable for the 10 Ω cm device at 77 K (Fig. 3). Where the devices approached high injection, the corresponding data were excluded from the analysis.

B. Saturation current I_{01}

The values of I_{01} , determined by fitting Eq. (1) to the data in Figs. 3 and 4, are given in Tables I and II together with the associated 1σ uncertainty for the 10 and 2 Ω cm devices, respectively. The uncertainty in I_{01} due to its extraction from the I - V data is estimated to vary from 2% to 5% in going from 300 to 77 K, due to the dominance of the ideal component. An additional uncertainty of 0.5% in I_{01} was also included which arises from the fringing field corrections discussed in Appendix A. A further uncertainty arises in the extracted value of I_{01} due to any uncertainty in the measurement of the device temperature. As outlined in Sec. III the Pt resistor sensor and resistance meter is esti-

TABLE II. Saturation current I_{01} , ionized dopant density N_A^- , minority-carrier electron diffusion constant D_n , and diffusion length correction factor $\omega \coth \omega$ for the 2 Ω cm device, as a function of temperature from 77 to 300 K.

T (K)	I_{01} (A)	N_A^- (10^{15} cm^{-3})	D_n (cm^2/s)	$\omega \coth \omega$
77.4	$1.49(25) \times 10^{-69}$	2.74(78)	53.3(210)	1.051(51)
100.1	$2.86(42) \times 10^{-52}$	4.77(75)	52.3(189)	1.032(32)
126.1	$5.77(73) \times 10^{-40}$	5.99(51)	52.9(172)	1.021(21)
150.4	$3.42(37) \times 10^{-32}$	6.43(42)	51.9(149)	1.015(15)
200.3	$5.10(39) \times 10^{-22}$	6.70(40)	45.6(98)	1.010(10)
249.6	$7.18(35) \times 10^{-16}$	6.76(40)	37.6(54)	1.008(8)
275.0	$1.43(6) \times 10^{-13}$	6.78(40)	34.3(36)	1.008(8)
300.0	$1.18(3) \times 10^{-11}$	6.78(40)	31.4(22)	1.007(7)

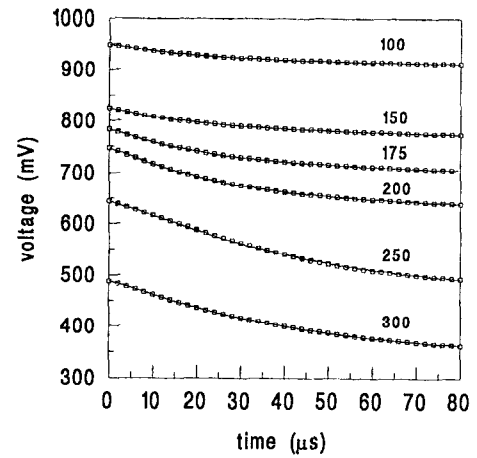


FIG. 5. Open-circuit voltage decay signals for the 10 Ω cm device as a function of temperature (100, 150, 175, 200, 250, 300 K). The experimental results (solid line) are plotted together with a theoretical curve (\square) which is fitted to the data.

mated to give a temperature measurement accurate to within 0.1 K. However, temperature gradients across the device may increase this uncertainty. Temperature gradients were monitored by having temperature sensors mounted directly above and below the device. From this the uncertainty in the device temperature was conservatively estimated to vary from 0.2 to 0.4 K in the range 300–77 K.

The value of I_{01} depends very strongly on temperature due to its squared dependence on n_i [Eqs. (A4) and (A5)]. In the worst case at 77 K this causes a variation in I_{01} of $\sim 300\%/K$ due to the rapid change in n_i as temperature decreases.³ At 300 K this variation is far less (about 17%/K); however, the uncertainty in the extracted value of I_{01} was found to be much smaller as explained below. Simulated I - V data was generated for temperatures $T - \Delta T$, T , and $T + \Delta T$. Equation (1) was then fitted to the data using a fixed temperature T . The variation in the extracted I_{01} due to temperature uncertainty was $\sim 40\%/K$ at 77 K and $\sim 11\%/K$ at 300 K. This reduction in sensitivity is because the value of I_{01} depends far more strongly on the value of T used in the fitting procedure than it does on the actual I - V data being analyzed. The total uncertainty in I_{01} therefore varies from between 3% and 17% for 300–77 K.

C. Minority-carrier electron diffusion constant D_n

Shown in Figs. 5 and 6 are the OCVD signals as a function of temperature, obtained for the 10 and 2 Ω cm devices respectively. The experimental results are plotted together with a theoretical curve fitted to the data, which is discussed below. At all temperatures the early stages of the signal show the voltage decreasing linearly with time, characteristic of ideal decay. After this linear region the decay is slower and is approximately exponential, characteristic of junction capacitance. The results at the lower temperatures display the smallest linear region in the decay signal. This occurs because the decay time in the base τ_0 decreases as the temperature decreases. This reduction in τ_0 as tem-

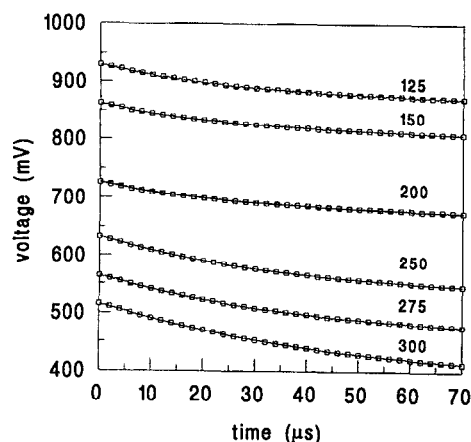


FIG. 6. Open-circuit voltage decay signals for the 2 Ω cm device as a function of temperature (125, 150, 200, 250, 275, 300 K). The experimental results (solid line) are plotted together with a theoretical curve (\square) which is fitted to the data.

perature decreases is due to the increase in (i) the minority-carrier electron mobility, (ii) recombination in the emitter, and to a lesser extent (iii) the decrease of the bulk lifetime τ_b [refer to Eq. (B12)]. The latter two effects will be more fully discussed below. As a result the region of linear decay becomes less as the temperature decreases and the capacitance begins to dominate the signal. This limits the usefulness of this technique for determining D_n to the higher temperatures.

The OCVD signals were analyzed by fitting to the data an ideal curve generated by numerically solving Eq. (B13) with the variable parameter being the decay time τ_0 . An improved fit to the data was obtained by allowing the base ionized dopant density N_A to also vary to improve the modeling of the capacitance-dominated region. This had little effect on the extracted value of the decay time. However, at temperatures at or below 125 K it was found that the OCVD signals were so dominated by the junction capacitance that a meaningful decay time could not be extracted. At higher temperatures the extracted decay time τ_0 was used to calculate the minority-carrier electron diffusion constant D_n using Eq. (3). This method of analysis was confirmed using the semiconductor device analysis program PC-1D.¹¹ Using this program, ideal OCVD signals could be generated which included the effects of junction capacitance and emitter recombination. These ideal curves were then analyzed as described above and the resulting value of D_n was in agreement with the value set within PC-1D, to within 3%.

As will be discussed in a subsequent section, the emitter saturation current I_{0e} becomes an increasingly larger component of I_{01} as the temperature decreases. However, as a value of I_{0e} could be determined for these devices it was possible to take into account the effect of recombination in the emitter on the OCVD signal by solving Eq. (B9). Minimum values of the bulk lifetimes at 300 K for these devices were estimated to be 760 and 1300 μ s for the 2 and 10 Ω cm devices, respectively. The method used to

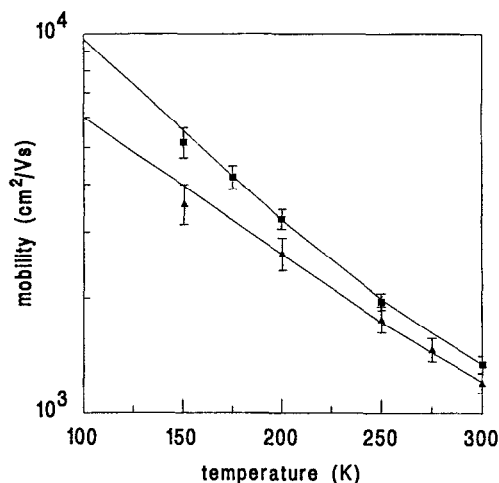


FIG. 7. Minority-carrier electron mobility as measured in this work as a function of temperature for the 10 (\blacksquare) and the 2 Ω cm device (\blacktriangle). The solid line is the majority-carrier electron mobility reported by Li and Thurber (see Ref. 12).

determine the variation of lifetime with temperature will also be discussed below. Hence, by using Eq. (3) it was possible to determine the minority-carrier electron diffusion constant from the OCVD signals. The results are shown in Fig. 7 where the minority-carrier electron mobility μ_n is plotted as a function of temperature. Also shown are calculated majority-carrier mobility results, at an equivalent ionized dopant density. The majority-carrier results are based on the calculated values reported by Li and Thurber.¹² The values have been lowered by 3% and 6%, for the 10 and 2 Ω cm samples respectively, across the whole temperature range, to bring the calculated values into agreement with later experimental values at room temperature.¹³ In a recent review of majority-carrier mobility these values were determined to be the most accurate.³

At lower temperatures the uncertainty in the present values increases due to the decrease in the linear section of the decay and the increasing effect of emitter recombination. The uncertainty in the bulk lifetimes introduces an uncertainty in D_n , which in the worst case is less than 3%. As will be discussed below, the uncertainty in the value of I_{0e} is quite large. This introduces an uncertainty in the value determined for D_n which at 150 K is estimated to be 10%. Further uncertainty arises as the temperature decreases due to the dominance of the capacitance portion of the decay. However, the results presented show no significant departure from the majority-carrier values, for the temperature range investigated.

However, the question remains as to what is the value of the minority-carrier electron mobility below 150 K. Very few results have been published for this parameter as a function of temperature in the range 77–300 K.¹⁴ Some values have been reported by Morohashi, Sawaki, and Akasaki,¹⁵ who measured the minority-carrier electron mobility over this temperature range in *p*-type silicon for dopant densities ranging from 10^{13} to 5×10^{15} cm^{-3} . They used the time-of-flight (TOF) technique and found values

~30%–50% lower than the equivalent majority-carrier mobility for temperatures below 150 K. They attributed this to electron-hole (e - h) scattering and modeled their results using the McLean–Paige theory.¹⁶ The effect of e - h scattering was observed in their experiment because the electrons and holes drift in opposing directions, with momentum of similar magnitude. By using OCVD for our measurements, the electrons and holes move in the same direction, as the device is at open circuit. Also the minority-carrier electron velocity is much greater than the majority-carrier hole velocity as the devices are kept in low injection. Hence, the drag component of e - h scattering is negligible in our OCVD experiments.

In the case of dark I - V measurements, the holes move in the opposite direction to the electrons; however, as for the OCVD case the velocity of the holes is small. Further, it has been shown that mobility reduction by e - h scattering has no effect on the dc current flow in p - n junction devices in low injection.^{17,18} The transfer of momentum to the holes by the electrons is counter balanced by the production of an electric field to maintain charge neutrality.¹⁷ This electric field assists the electron flow and the net result is that the flow of the minority carrier electrons is the same as if e - h scattering was ignored.

Another mechanism which may cause the minority-carrier mobility to deviate from the majority-carrier values at low temperature is ionized dopant scattering. At high dopant concentrations, it is now well established that minority-carrier mobility is greater than the majority-carrier values due to less effective scattering by the ionized dopant.¹⁴ This is because the scattering is repulsive for minority carriers but attractive for majority carriers.¹⁹ However Kay and Tang²⁰ have shown using Monte Carlo techniques that this effect is insignificant for dopant densities $< 10^{16} \text{ cm}^{-3}$ at 77 K. Hence, in order to model the device characteristics presented here the mobility data of Li and Thurber¹² was used as this was in agreement with the results presented here for $T > 150 \text{ K}$ and could be extended to lower temperatures. The values used are shown in Tables I and II along with the associated 1σ uncertainty. Above 150 K the uncertainties are based on the difference between the results presented here and the majority-carrier values. For lower temperatures greater uncertainty has been assigned to this parameter, due to the lack of experimental results. The uncertainties were estimated to vary from 7% at 300 K to 20% and 40% at 77 K for the 10 and 2 $\Omega \text{ cm}$ devices, respectively.

D. Ionized dopant density N_A^-

The ionized dopant density in the p region of the devices was determined from four-point-probe resistivity measurements upon the wafer substrates at 23 °C, as described previously.⁷ The resistivity measurements were converted to dopant densities N_A at 300 K using the mobility results of Thurber and co-workers¹³ and the more recent results of Sproul and co-workers.¹⁴ An average of the two values was used. The difference in the mobility values of Ref. 13 and 14 for these devices is less than 4%. The more recent mobility measurements are made on un-

processed float-zone wafers and are believed to be accurate to within 5%.¹⁴ The estimated uncertainty in the final value of N_A at 300 K is 6%. The ionized dopant density N_A^- was calculated using

$$N_A^- = \frac{N_A}{1 + g \exp[(E_A - E_F)/kT]}, \quad (4)$$

where E_A is the acceptor ionization energy, E_F is the Fermi energy, and g is the degeneracy factor for acceptor levels. A more complete description is given elsewhere.⁷ A value of 4 is commonly assigned to g . This arises from the electron spin degeneracy (a factor of 2) as well as the double degeneracy present in the energy bands at the maximum energy in the valence band (i.e., the acceptor energy levels have the same degeneracy as the light- and heavy-hole bands). Li²¹ has suggested that g should include an additional factor $2 \exp(-\Delta/kT)$ which arises from considering the contribution from the split-off band. As a conservative estimate, the degeneracy factor was assigned a value of $g = 4 \pm 2$ which covers the value cited by Li. The total uncertainty in N_A^- varied from 6% to 28% for the 10 and 2 $\Omega \text{ cm}$ device and 6% to 40% for the 2 $\Omega \text{ cm}$ device in going from 300 to 77 K. The values determined for this parameter and the associated 1σ uncertainty is given in Tables I and II.

E. Minority-carrier electron diffusion length L_n

One of the major benefits of the device structure employed here is that due to the high effective rear surface recombination velocity, the value of L_n need not be determined accurately. The term $\omega \coth \omega$ in Eq. (2) will be close to unity provided $L_n \gg W$. In our previous study,⁷ upper and lower bounds could be placed on L_n by comparison of the saturation currents of the present devices with those of conventional high-efficiency PERC cells. The lower bound on the bulk lifetimes determined in this way was 760 μs and 1.3 ms for the 2 and 10 $\Omega \text{ cm}$ devices respectively at 300 K. The same approach could not be used here because, unlike the situation near room temperature, the saturation current for the PERC cells at lower temperatures becomes increasingly dominated by emitter recombination. Therefore, the temperature dependence of L_n was calculated from published data of the temperature dependence of the minority-carrier electron lifetime τ_b and the value of D_n determined above (as $L_n^2 = D_n \tau_b$).

For the dopant densities considered here, the minority-carrier lifetime is dominated by defect recombination as described by the Shockley–Read–Hall (SRH) theory.²² The lifetime depends on the capture cross section of the defect σ , the thermal velocity of the electron v_{th} , the density of defects N_T , and on the energy level of the defect or trap E_T .²² Experimentally, electron lifetimes τ_n have been observed to vary approximately as

$$\tau_n = \tau_{n*} (T/300)^x, \quad (5)$$

where τ_{n*} is the lifetime at 300 K and x is a constant. Dziejior and Schmid²³ have observed lifetimes to vary between 77 and 300 K with $x = 1.7$ and Hacker and Han-

gleiter (in an unpublished work cited by Swanson and Swirhun²⁴) have observed $x=1$. Accordingly, $x=2$ was used to determine a lower bound for τ_n , and hence an upper bound on $\omega \coth \omega$. The minimum value that $\omega \coth \omega$ can have is unity. This was used as the lower bound for this parameter. The lower and upper bounds determined in this way allowed $\omega \coth \omega$ and its uncertainty to be calculated as a function of temperature. The resulting values are given in Tables I and II for the two devices. In the worst case $\omega \coth \omega$ differs from unity by only 5%.

F. Quasi-neutral width W and cell area A

The cell area A was determined using a calibrated optical microscope and found to be equal to $4.00(3) \text{ cm}^2$. The digits in parentheses represent the estimated one-standard-deviation (1σ) uncertainty in the last digit of the previous value. This convention will be adopted throughout this article. The thickness of the silicon substrates was determined using a micrometer. From this thickness, the width of the quasi-neutral p region W was determined by subtracting the depth of the p - n junction (based on spreading resistance measurements for similarly processed devices) and calculated values for the depletion layer widths associated with the front p - n and rear Schottky junction.⁹ The temperature dependence of the depletion widths is weak. The value of W for both the 10 and 2 $\Omega \text{ cm}$ devices is $284(3) \mu\text{m}$.

G. Emitter saturation current I_{0e} and band-gap narrowing ΔE_g

Near room temperature I_{0e} is small in comparison to I_{01} and was previously estimated from the high open-circuit voltages (or low saturation currents) of PERC cells.⁷ As the temperature decreases, however, I_{0e} increases relative to I_{01} due to the effect of band-gap narrowing (BGN) in the more heavily doped emitter. This increase in I_{0e} has been observed from the I - V characteristics for a high-efficiency PERC cell at low temperatures. Near 77 K the PERC cell had a saturation current similar to the 2 $\Omega \text{ cm}$ device investigated here. Hence the approach adopted in analyzing the data was to treat both I_{0e} and n_i as unknowns. At the same temperature, the results for the 10 and 2 $\Omega \text{ cm}$ devices can be substituted into Eq. (2), yielding two equations. Solving these equations yields values for n_i and I_{0e} . As I_{01} varies with temperature predominantly as n_i^2 then where the device temperatures differed slightly (T_1 for the 2 $\Omega \text{ cm}$ device and T_2 for the 10 $\Omega \text{ cm}$ device), the saturation current for the 2 $\Omega \text{ cm}$ device was multiplied by a factor $[n_i(T_2)/n_i(T_1)]^2$. The values used for n_i were those reported by Green.³ Since the temperature difference is small, this introduces a negligible error in comparison to the other uncertainties.

The assumptions in this approach are that I_{0e} is the same for the two devices and that there is no band-gap narrowing in the base region of the devices. That I_{0e} is the same for the two devices is believed to be a good assumption as these devices were fabricated simultaneously. BGN

is usually discussed in conjunction with more heavily doped regions (i.e., greater than 10^{17} cm^{-3}). It is in this area that most work has been concentrated, both experimentally^{25,26} and theoretically.^{27,28} In general BGN theories are usually developed for high doping concentrations and are only applicable for dopant densities above 10^{18} cm^{-3} .^{27,28} A limited amount of experimental data exists for lower doping densities. Room-temperature measurements on transistors with a p -type base region indicate some BGN at dopant densities N , as low as $4 \times 10^{15} \text{ cm}^{-3}$.²⁵ However, these values are of the order of $\pm 5 \text{ meV}$ and similar values are obtained at dopant densities of 10^{17} cm^{-3} .²⁵ However, since these values are of the same magnitude as the experimental uncertainties it is common to fit expressions of the form of $\Delta E_g \propto \ln(N/N_0)$ to the experimental data. This gives zero BGN for dopant densities below $N_0 \approx 10^{17} \text{ cm}^{-3}$.²⁶

Our previous measurements at 300 K indicated a slight increase in the values of n_i as doping in the p -region increased,⁷ which would be consistent with a small amount of band-gap narrowing for substrates doped in the 10^{15} – 10^{16} cm^{-3} range. An estimate of an upper and lower bound for the band-gap narrowing in the 2 $\Omega \text{ cm}$ device can be made. From the high open-circuit voltages of PERC solar cells with similar emitters, a value of $I_{0e} = 0.45(17) \text{ pA}$ at 300 K can be determined. Using this value of I_{0e} to analyze the previous n_i data as a function of doping reported at 300 K for these devices⁷ yields a value of between 0 and 2.5 meV at 300 K for the BGN in the base of the 2 $\Omega \text{ cm}$ device. This has a small effect near room temperature but becomes increasingly significant as the temperature decreases. These bounds were used in all subsequent calculations as BGN should decrease as the temperature and hence the carrier density decreases. This decrease has been observed experimentally.²⁴ Hence, allowing for a 20% uncertainty in I_{0e} between the devices and the bounds on BGN discussed above, the approach outlined here allows the determination of the intrinsic carrier concentration and the emitter saturation current from the device measurements, as a function of temperature. The values for I_{0e} determined in this way can be described by an expression of the form $I_{0e} = An_i^2 \exp(\Delta E/kT)$, where $A = 1.93 \times 10^{-33} \text{ A cm}^6$ and $\Delta E = 41.8 \text{ meV}$. This value for ΔE is equivalent to the band-gap narrowing reported in n -type silicon for dopant densities near $2 \times 10^{18} \text{ cm}^{-3}$.²⁵ This is similar to the peak dopant density at the surface of the emitters of these devices. The results for the intrinsic carrier concentration will be discussed in the following section.

V. DISCUSSION

Shown in Table III are the calculated values of n_i together with the associated 1σ uncertainties. Note the strong dependence on temperature, with the values of n_i varying by 30 orders of magnitude in going from 300 to 77 K. The values of the present work (saturation current) are compared to values calculated from band parameters in Table III. The band parameter values are calculated using the band-gap energy and density-of-states (DOS) effective

TABLE III. The intrinsic carrier concentration n_i of silicon as a function of temperature for two different methods. Saturation current: values determined from this work; and band parameters (Ref. 2). The three sets of results calculated from band parameters are based on valence-band density-of-states effective masses from different investigators.

T (K)	Units (cm^{-3})	Saturation current	Band parameters		
			Hensel	Madarasz	Humphreys
77.4	10^{-20}	3.10(84)	2.74(37)	2.83(38)	3.02(41)
100.6	10^{-11}	3.33(50)	2.80(35)	2.94(37)	3.16(39)
125.9	10^{-05}	3.84(47)	3.48(42)	3.69(44)	3.95(47)
151.2	10^{-01}	4.61(49)	4.32(50)	4.60(54)	4.94(58)
200.3	10^{+04}	5.10(45)	4.95(56)	5.32(61)	5.73(65)
250.3	10^{+07}	7.33(54)	7.29(82)	7.83(88)	8.46(95)
275.3	10^{+09}	1.08(7)	1.07(12)	1.15(13)	1.25(14)
300.0	10^{+10}	0.99(6)	1.00(11)	1.08(12)	1.17(13)

masses as reported in a recent review by Green³ according to the equation

$$n_i^2 = N_C N_V e^{-E_g/kT}. \quad (6)$$

In this expression E_g is the energy band gap, and N_C and N_V are the effective densities of states in the conduction and valence bands, respectively. N_C and N_V are functions of the temperature and the DOS effective masses in the conduction and valence bands, m_{dc}^* and m_{dv}^* , respectively.³ In Table III, three different sets of values of n_i are presented. These are based on different values reported for the valence-band DOS effective mass, m_{dv}^* , as reported by Humphreys,²⁹ Hensel (from an unpublished work of Hensel cited by Humphreys²⁹), and Madarasz and co-workers.⁶ The differences in m_{dv}^* arise from differences in interpretation of the cyclotron resonance data at low temperature and the methods used to calculate the temperature dependence of m_{dv}^* .³ This temperature dependence arises from the nonparabolicity of the valence bands, especially the heavy-hole band. It is this parameter which contributes the greatest uncertainty to the values of n_i determined from the band parameters, with only a 1 meV uncertainty in E_g . The uncertainty in the values of n_i calculated in this way is given in Table III.

From Table III, it can be seen that the saturation current values of n_i are in reasonable agreement with the values determined from band parameters across the range of 300 to 77 K. At the higher temperatures the agreement is best with the values as reported by Hensel, as noted previously for the results at higher temperatures;⁷ however, as the temperature decreases the present values decrease less slowly than the values of Hensel. At the very lowest temperature, the values reported here are greater than the highest band parameter value as reported by Humphreys. The experimental uncertainty of the present method is greatest at these lowest temperatures so exact agreement with any of the band parameter results should not be expected. Therefore, the results presented here and at higher temperatures⁷ support the intrinsic carrier concentration values based on the effective mass values of Hensel. An expression for n_i , which is a fit to the values calculated using the effective mass values of Hensel, and the band-gap

energy E_g based on the work of Bludau, Onton, and Heinke³⁰ and Macfarlane *et al.*³¹ as cited by Green,³ is given by

$$n_i = 1.640 \times 10^{15} T^{1.706} e^{-E_g/2kT}. \quad (7)$$

This expression describes the above data to within 1% and is valid across the range 77–400 K. Evaluating this expression at 77 K gives $n_i = 1.72 \times 10^{-20} \text{ cm}^{-3}$ and at 300 K, $n_i = 1.00 \times 10^{10} \text{ cm}^{-3}$.

VI. CONCLUSIONS

The first direct measurements of the intrinsic carrier concentration in the temperature range below 250 K are reported in this article. Our results are in good agreement with the values reported by Green based on band parameter calculations.³ In the temperature range of 200–300 K the present results are in agreement to within 5% with the values of n_i based on the effective mass values of Hensel, as cited by Humphreys.²⁹ At lower temperatures the present results tend towards slightly higher values ($\sim 10\%$ – 15% higher) but the Hensel values are still within the experimental uncertainties of the present results. We also report measurements of the minority-carrier electron mobility in the range 150–300 K, which are in good agreement with the majority-carrier values based on those reported by Li and Thurber,¹² modified as described in this article.

ACKNOWLEDGMENTS

The authors thank Professor John Storey and Mark Unewisse for access to the cryogenic system located within the School of Physics, University of New South Wales. This work was partly supported by the Australian Research Council and Sandia National Laboratories. The Centre for Photovoltaic Devices and Systems is supported by the Australian Research Council Special Research Centres Scheme and Pacific Power. A.B.S. gratefully acknowledges the financial support of an Australian Postgraduate Research Award and a Supplementary Engineering Scholarship.

APPENDIX A: THEORY OF I - V CHARACTERISTICS

In this appendix we outline the derivation of Eqs. (1) and (2). The devices can be modeled using a modified Ebers–Moll equivalent circuit for a bipolar transistor, shown in Fig. 2. This model is appropriate due to the formation of a rectifying Schottky diode by evaporation of Al on the polished rear of the wafer.^{7,8} Al forms a Schottky barrier on p silicon with a relatively low barrier height of 0.4–0.6 eV.⁹ The sintering conditions, discussed above, produce partial shunting of this diode. That is, sintering of the Al layer creates a relatively low shunting resistance between the rear Al contact and the p substrate.⁸ The device structure can therefore be modeled by the circuit shown in Fig. 2, with the diffused p - n junction forming the emitter and the Schottky junction forming the collector in the Ebers–Moll equivalent circuit.

The p - n junction is modeled by two diodes having ideality factors of unity and n , where n is greater than unity.³² I_{01} and I_{0n} are the saturation currents associated with each of these two diodes. I_{RS} is the saturation current associated with the rear Schottky junction. All three saturation currents have to be calculated with the other junction shorted, i.e., the junction area replaced by an infinite recombination velocity surface.⁹ Also shown are the normal current-controlled current sources of the Ebers–Moll equivalent circuit.⁹ These current sources have values of $\alpha_F I_F$ and $\alpha_R I_R$, determined by the current in the opposite junction multiplied by the injection efficiency α of the opposite junction.⁹ In addition to the standard Ebers–Moll circuit described thus far, a shunt resistance R_{SH} is added to model the shunting resistance discussed above. A series resistance R_S is also included to model any resistive losses due to resistances associated with the cell metalization or substrate.

The dark I - V characteristics can be derived based on the above equivalent circuit. When the top junction is forward biased, the rear junction is reversed biased and hence the current through the rear Schottky diode I_R is essentially zero. Hence the measured current I will be equal to the current through the front junction I_F . The voltage drop across the rear junction ΔV_R is

$$\Delta V_R = I(1 - \alpha_F)R_{SH}. \quad (\text{A1})$$

Assuming that the injection efficiency α_F is constant for all bias conditions investigated, then for an applied voltage V , the voltage across the p - n junction is

$$V - I[R_{SH}(1 - \alpha_F) + R_S] = V - IR', \quad (\text{A2})$$

where R' is an effective resistance. Therefore the forward biased dark I - V characteristics can be described by

$$I = I_{01}(e^{q(V - IR')/kT} - 1) + I_{0n}(e^{q(V - IR')/nkT} - 1). \quad (\text{A3})$$

The ideality factor n describes recombination within the space-charge region at the top junction and depleted (or inverted) surface regions. This description is valid for devices operating in low injection only. The thermal voltage kT/q equals 25.852 16(22) meV at 300 K using rec-

ommended values of the physical constants.³³ I_{01} is strongly dependent upon n_i .⁹ It is this parameter that is extracted from the experimental I - V characteristics and then a value for n_i calculated. For a one-dimensional model of the cell the relationship is given by

$$I_{01} = I_{0b} + I_{0e}, \quad (\text{A4})$$

where

$$I_{0b} = (AqD_n n_i^2 / WN_A^-)(\omega \coth \omega). \quad (\text{A5})$$

I_{0b} is the saturation current associated with the p region and rear contact (i.e., the “base” region) while I_{0e} is the saturation current associated with the front n -type surface diffusion and metalization (i.e., the “emitter” region). A is the area of the cell; q is the electronic charge; D_n and L_n are the minority-carrier electron diffusion constant and diffusion length respectively; N_A^- is the ionized dopant concentration in the p -type substrate; W is the width of the quasi-neutral p region (Fig. 1), and ω is equal to W/L_n .

The above analysis is valid if the current in the device varies in only one dimension. As analyzed previously,⁷ there is some two-dimensional current in these devices. This arises from minority-carrier electron current spreading from the periphery of the p - n junction as it is injected into the base region. This “fringing effect” was calculated to increase the one-dimensional saturation current I_{0b} by only 2.5% for the devices considered here.⁷ This small correction factor is estimated to be accurate to within 0.5%. Other mechanisms that could affect the value of I_{01} arise from consideration of the surface regions surrounding the top n diffused region. This is a 4 cm² area surrounded by the oxidized surface of the p -type substrate. Inversion or depletion of the p -type surface could introduce unwanted effects in the I - V characteristics. This has been analyzed for the illuminated case⁷ and it was concluded that these surface effects, if present at all, would introduce an additional component to the I - V characteristics with an ideality factor $n > 1$. The same arguments apply to the dark I - V characteristics. In the analysis presented subsequently only the current component with unity ideality factor is extracted and used in calculating the intrinsic carrier concentration. Hence, inverted or depleted surfaces have no effect on the results.

Rearranging Eqs. (A4) and (A5) and including the “fringing field” effect as discussed above, the intrinsic carrier concentration is then given by

$$n_i = \left(\frac{WN_A^- (I_{01} - I_{0e}) / 1.025}{AqD_n(\omega \coth \omega)} \right)^{1/2}. \quad (\text{A6})$$

APPENDIX B: OCVD THEORY

In this appendix we outline the derivation of Eq. (3). The approach taken is to solve the continuity equation firstly for the case where the OCVD signal is determined solely by recombination of minority carriers in the base of the cell. Deviations of the decay from this ideal case, due to emitter recombination and junction capacitance, are then treated.

Dhariwal and Vasu³⁴ have solved the continuity equation to obtain the excess minority-carrier electron concentration in the p -type base $\Delta n(x,t)$, when recombination in the base dominates. The solution for $\Delta n(x,t)$ is simplified for certain values of the rear-surface recombination velocity S_R .³⁴ For the devices analyzed here, the rear Schottky diode causes the device characteristics to be identical to a device with $S_R \rightarrow \infty$. In this case $\Delta n(x,t)$ becomes³⁴

$$\Delta n(x,t) = \sum_{m=0}^{\infty} \frac{2J_F \tau_m}{qW} (-1)^m e^{-t/\tau_m} \sin[\alpha_m(W-x)], \quad (B1)$$

where

$$1/\tau_m = (1/\tau_b) + \alpha_m^2 D_n \quad (B2)$$

and

$$\alpha_m = (2m+1)\pi/2W. \quad (B3)$$

J_F is the initial current density flowing during forward bias, W is the width of the quasineutral base region (Fig. 1.), τ_m is the decay time of the m th decay mode, and α_m is the m th eigenvalue, defined by Eq. (B3). The voltage across the p - n junction $V_j(t)$ is related to the excess minority-carrier electron concentration at the edge of the depletion region $\Delta n(0,t)$ by

$$V_j(t) = \frac{kT}{q} \ln \left(\frac{\Delta n(0,t)}{n_0} + 1 \right), \quad (B4)$$

where n_0 is the minority-carrier electron concentration in the base at thermal equilibrium. Also we have assumed for simplicity that the ideality factor is unity. This assumption is a very good one for the devices investigated here as is shown from experiments described in Sec. IV.

Note that the decay is characterized by an infinite number of decay times. However, it can be seen from Eqs. (B2) and (B3) that the longest decay time and the term with the largest amplitude occurs for the principal mode, $m=0$. It has a decay time given by

$$\frac{1}{\tau_0} = \frac{1}{\tau_b} + \left(\frac{\pi}{2W} \right)^2 D_n. \quad (B5)$$

The higher-order modes rapidly die out and the minority-carrier electrons then decay via the principal decay mode. In this case, as the carrier density is decaying exponentially with a single decay time τ_0 , the voltage decay is linear. Calculations based on Eq. (B1) show that $\Delta n(x,t)$ is, to within 1%, dominated by the principal mode after a time equal to $\sim 50\% \tau_0$ over the range of temperatures investigated. Typically τ_0 is of the order of 10 μ s or less. Therefore, by excluding the initial 5 μ s of the signal the principal decay time can be extracted.

There are several mechanisms that can cause the OCVD signal to depart from the description given above. For the devices investigated here the most important is junction capacitance followed by emitter recombination, and last, series resistance. Series resistance in the device simply introduces an initial voltage drop once the forward-

bias current stops flowing. The decay after this time is then unaffected by the resistance as the device is open-circuited.

Recombination in the emitter affects the decay if it is a significant fraction of the recombination in the device.³⁵ Usually, the decay time of the minority-carrier holes in the emitter τ_p is one or two orders of magnitude less than the decay time τ_0 in the base. Hence, during the initial stages of the OCVD signal, the initial excess carriers in the emitter decay very rapidly while very few carriers in the base region recombine. As the junction voltage remains while there are excess minority-carrier electrons in the base, holes are injected from the p region into the emitter. This is because $p_n = p_0 \exp(qV_j/kT)$, where p_n is the hole concentration and p_0 is the equilibrium hole concentration at the edge of the depletion layer in the emitter. As all the excess electrons that were initially in the emitter have recombined, electrons from the base region must also be supplied to the emitter in order for the holes to recombine. As $\tau_p < \tau_0$ then this increases the rate at which the excess electrons in the device decay compared to the situation where no recombination occurs in the emitter.

Since the quasistatic approximation holds in the emitter during OCVD decay³⁵ the flow of electrons and holes into the emitter region can be described by electron- and hole-current densities J_n and J_p given by

$$J_n = -J_p = J_{0e}(e^{qV_j(t)/kT} - 1). \quad (B6)$$

In this expression J_{0e} is the emitter saturation current density and we have assumed that no recombination occurs in the depletion region which is a good assumption for the devices investigated here. The electron current can alternatively be expressed in terms of a recombination velocity S_F at the edge of the depletion region in the base, given by

$$S_F = N_A^- J_{0e} / qn_i^2. \quad (B7)$$

The solution of the continuity equation is simplified if the x axis is defined such that the edge of the depletion layer in the p region is at $x = -\delta$ and therefore the rear contact is at $x = W - \delta = W'$, where W' is the effective width of the quasineutral p region. The boundary conditions for the continuity equation now become

$$D_n \frac{\partial \Delta n}{\partial x} = S_F \Delta n \big|_{x=-\delta}$$

and

$$-D_n \frac{\partial \Delta n}{\partial x} = S_R \Delta n \big|_{x=W'}.$$

Applying these boundary conditions to obtain a solution for $\Delta n(x,t)$ yields equations which define the eigenvalues α_m of the solution. As for the ideal case there is an infinite number; however, for small values of S_F and $S_R \rightarrow \infty$ the solution for $\Delta n(x,t)$ varies little from that given by Eq. (B1). The decay is dominated by the principal decay time τ_0 with the only difference being that τ_0 is slightly lower than the value given by Eq. (B5). Hence, only the principal eigenvalue α_0 need be found. This is done by solving simultaneously the following equations:

$$\cot(\alpha_0\delta) = \alpha_0 D_n / S_F \quad \text{and} \quad \cot(\alpha_0 W') = \alpha_0 D_n / S_R. \quad (\text{B9})$$

Since S_F is small and S_R is essentially infinite then α_0 is given by

$$\alpha_0 = \sqrt{S_F / D_n} \delta = \pi / 2 W', \quad (\text{B10})$$

which upon rearrangement for δ , gives

$$\delta = \frac{S_F}{D_n} \left(\frac{2W'}{\pi} \right)^2 \approx \frac{I_{0e}}{I_{0b}} \frac{4W}{\pi^2}. \quad (\text{B11})$$

This expression yields a quadratic in δ . For the case where $W \approx W'$, δ can be estimated by the second expression where I_{0b} is the saturation current of the base region given by Eq. (A5) (with $\omega \coth \omega$ set to unity). The decay time of the principal mode τ_0 is easily evaluated and is given by

$$\frac{1}{\tau_0} = \frac{1}{\tau_b} + \left(\frac{\pi}{2W'} \right)^2 D_n. \quad (\text{B12})$$

As is shown in Sec. IV recombination in the emitter is insignificant for these devices except at the very lowest temperatures investigated. Since the emitter saturation current density can be determined from the data presented in Sec. IV, the effect on the OCVD signals can be treated.

When I_{0e} does become a significant fraction of I_{01} this changes the conditions stated above as to how long the carrier profile takes to be dominated by the principal decay mode. The maximum difference will occur for the case where I_{0e} is so large that $S_F = S_R \rightarrow \infty$. In this case $\delta = W' = W/2$. This situation is very similar to that treated by Luke and Cheng,³⁶ who analyze the decay of excess carriers excited by a laser pulse with both surfaces having a high surface recombination velocity.³⁶ Their calculations indicate that the time taken for the excess carrier concentration to be dominated by the principal decay mode occurs after a time equal to approximately $1.3\tau_0$.³⁶ However this increase over the ideal case ($\sim 0.5\tau_0$) is offset by the concomitant decrease in τ_0 due to (i) the emitter recombination and (ii) the increase in mobility at lower temperatures.

Experimentally, the worst case analyzed here occurs for the 2 Ω cm device at 150 K. In this case $I_{0e}/I_{01} \approx 0.35$; $\tau_0 \approx 6$ μ s, and $1.3\tau_0 \approx 8$ μ s. Therefore, as a conservative approach the initial 10 μ s of the signal was not analyzed. However, varying this time between 5 and 10 μ s caused the final value of τ_0 to vary by less than 2%. This indicates that the time taken for the principal decay mode to dominate the OCVD signal is negligibly affected by emitter recombination.

Junction capacitance also causes a departure from the ideal decay. Generally this makes the OCVD signal decay more slowly at lower voltages and the signal is no longer linear. This effect has been analyzed by Mahan and Barnes³⁷ using charge storage analysis. They consider the decay of the total excess minority-carrier charge in the quasi-neutral base region per unit area $Q_n(t)$ during open-circuit voltage decay. This can be found by the solution of the following equation:

$$\frac{Q_n(t)}{\tau_e} + \frac{dQ_n(t)}{dt} + \frac{CdV_j(t)}{dt} = 0. \quad (\text{B13})$$

The first term describes the recombination of the minority carriers in the base region with an effective lifetime τ_e . When the OCVD signal is dominated by the principal decay time τ_0 then $\tau_e = \tau_0$. The second term is simply the rate of change of $Q_n(t)$, while the third term describes the effect of the junction capacitance C on the decay. The capacitance is a function of the voltage across the junction $V_j(t)$ and for the depletion layer approximation, for an abrupt junction, C is given by³⁷

$$C = \sqrt{q\epsilon N_A / 2[\psi_0 - V_j(t)]}, \quad (\text{B14})$$

where ϵ is the permittivity of silicon and ψ_0 is the built-in potential. The excess charge in the base is related to the junction voltage by

$$V_j(t) = \frac{kT}{q} \ln \left(\frac{Q_n(t)}{Q_{n0}} + 1 \right), \quad (\text{B15})$$

where Q_{n0} is the base reference charge per unit area. In their treatment Mahan and Barnes assume that the quasi-static approximation holds for the decay of minority carriers in the base region. That is, the minority-carrier profile across the base region at any instant in time has the same profile as the equilibrium case where $V_j = V_j(t)$. This is not true for the decay where $S_R \rightarrow \infty$ as is the case here. As discussed above, for the OCVD signals analyzed here the minority-carrier profile is dominated by the principal mode. That is, the profile is a quarter sine wave across the device. For this situation and for the narrow-base case where $W < L_n$ then Q_{n0} is given by

$$Q_{n0} = 2qWn_i^2 / \pi N_A. \quad (\text{B16})$$

Junction capacitance has no effect on the time taken for the carrier profile to be dominated by the principal decay mode. This is because the boundary condition at the edge of the depletion layer is unchanged by the capacitance. That is, S_F is unaffected by the capacitance and is determined solely by the effect of emitter recombination as discussed above.

Equation (B13) was solved numerically and fitted to the experimental data by varying the effective lifetime. As is shown in Sec. IV the solution describes the experimental data quite well. This allows the principal decay time τ_0 to be extracted from the experimental OCVD signal and hence the minority-carrier electron mobility could be determined.

¹S. Selberherr, IEEE Trans. Electron Devices ED-36, 1464 (1989).

²M. Chrzanowska-Jeske and R. C. Jaeger, IEEE Trans. Electron Devices ED-36, 1475 (1989).

³M. A. Green, J. Appl. Phys. 67, 2944 (1990).

⁴A. Herlet, Z. Angew. Phys. 9, 155 (1957).

⁵H. D. Barber, Solid-State Electron. 10, 1039 (1967).

⁶F. L. Madarasz, J. E. Lang, and P. M. Hemeger, J. Appl. Phys. 52, 4646 (1981).

⁷A. B. Sproul and M. A. Green, J. Appl. Phys. 70, 846 (1991).

⁸M. A. Green, A. W. Blakers, J. Zhao, A. M. Milne, A. Wang, and X. Dai, IEEE Trans. Electron Devices ED-37, 331 (1990).

- ⁹S. M. Sze, *Physics of Semiconductor Devices*, 2nd ed. (Wiley, New York, 1981).
- ¹⁰M. A. Green, *Sol. Cells* **11**, 147 (1984).
- ¹¹P. A. Basore, in *IEEE Photovoltaic Specialists Conference*, 1991, p. 299.
- ¹²S. S. Li and W. R. Thurber, *Solid-State Electron.* **20**, 609 (1977).
- ¹³W. R. Thurber, R. L. Mattis, and Y. M. Liu, *The Relationship Between Resistivity and Dopant Density for Phosphorus- and Boron-doped Silicon*, Nat. Bur. Stand., Spec. Publ. No. 400-64 (U.S. GPO, Washington, DC, 1981).
- ¹⁴A. B. Sproul, M. A. Green, and A. W. Stephens, *J. Appl. Phys.* **72**, 4161 (1992).
- ¹⁵M. Morohashi, N. Sawaki, and I. Akasaki, *Jpn. J. Appl. Phys.* **24**, 732 (1985).
- ¹⁶T. P. McLean and E. G. S. Paige, *J. Phys. Chem. Solids* **16**, 220 (1960).
- ¹⁷W. P. Dumke, *Solid-State Electron.* **28**, 183 (1985).
- ¹⁸W. Hänsh and G. D. Mahan, *J. Phys. Chem. Solids* **44**, 663 (1983).
- ¹⁹H. S. Bennet, *Solid-State Electron.* **26**, 1157 (1983).
- ²⁰L. E. Kay and T. W. Tang, *J. Appl. Phys.* **70**, 1475 (1991).
- ²¹S. S. Li, *Solid-State Electron.* **21**, 1109 (1978).
- ²²J. S. Blakemore, *Semiconductor Statistics* (Pergamon, Oxford, 1962).
- ²³J. Dziewior and W. Schmid, *Appl. Phys. Lett.* **31**, 346 (1977).
- ²⁴R. M. Swanson and S. E. Swirhun, Report No. SAND 87-7019, Sandia National Laboratories, Albuquerque, Nov., 1987.
- ²⁵D. B. M. Klassen, J. W. Slotboom, and H. C. de Graaf, *Solid-State Electron.* **35**, 125 (1992).
- ²⁶R. R. King and R. M. Swanson, *IEEE Trans. Electron Devices* **ED-38**, 1399 (1991).
- ²⁷S. C. Jain and D. J. Roulston, *Solid-State Electron.* **34**, 453 (1991).
- ²⁸A. Ghazali and J. Serre, *Solid-State Electron.* **28**, 145 (1985).
- ²⁹R. G. Humphreys, *J. Phys. C* **14**, 2935 (1981).
- ³⁰W. Bludau, A. Onton, and W. Heinke, *J. Appl. Phys.* **45**, 1846 (1974).
- ³¹G. G. Macfarlane, T. M. McClean, J. E. Quarraington, and V. Roberts, *Phys. Rev.* **111**, 1245 (1958).
- ³²I. Getreu, *Modeling the Bipolar Transistor* (Tektronix, Beaverton, OR, 1976).
- ³³E. R. Cohen and B. N. Taylor, *Codata Bull.* **63**, 1 (1986).
- ³⁴S. R. Dhariwal and N. K. Vasu, *Solid-State Electron.* **24**, 915 (1981).
- ³⁵U. C. Ray, S. K. Agarwal, and S. C. Jain, *J. Appl. Phys.* **53**, 9122 (1982).
- ³⁶K. L. Luke and L. J. Cheng, *J. Appl. Phys.* **61**, 2282 (1987).
- ³⁷J. E. Mahan and D. L. Barnes, *Solid-State Electron.* **24**, 989 (1981).